CHAPTER V

Structural, D.C Conductivity and Dielectric Studies of Barium Substituted $Bi_4V_2O_{11}$ Solid Solution

---

You cannot understand the glories of the universe without believing there is some Supreme Power behind it.

Stephen Hawking

5.1. Introduction

From our earlier study, it has been noticed that substitution of monovalent (Li) and divalent (Ca) cation at Bi-site of $Bi_4V_2O_{11}$ is favourable for enhancement of ionic conductivity. It was already mentioned that a wide range of cations have been substituted for V-site of the parent compound $Bi_4V_2O_{11}$, a few cations have been reported to substitute for Bi [**1-2**] and limited efforts have been devoted on structural and electrical characterization of Bi-site substituted BIMEVOX system. Moreover, no reports have been found for Ba substituted BIMEVOX on either V or Bi site. Our present work in this chapter is concerned with the compositional variation of structural and electrical properties of Ba doped, i.e., $Bi_{4-x}Ba_xV_2O_{11-\delta}$ ($0 \leq x \leq 0.4$) solid solutions.

5.2 Experimental

The series of compounds $Bi_{4-x}Ba_xV_2O_{11-\delta}$ ($0 \leq x \leq 0.4$) solid solutions were prepared by reacting stoichiometric mixtures of Bi_2O_3, V_2O_5 and $BaCO_3$. The details of the experimental technique for the preparation of the samples were discussed in **chapter-II.**

5.3. Results and discussion

5.3.1 X-ray diffraction

Fig 5.1 depicts the XRD patterns for the samples of the compounds $Bi_{4-x}Ba_xV_2O_{11-\delta}$ (x= 0, 0.1, 0.2, and 0.3). As described in the chapter-III and IV, the first two doped samples clearly exhibit orthorhombic α-polymorph distinguished by the characteristic doublets at $2\theta \approx 32°$, 48°, 54° and a weak reflection at $2\theta \approx 24°$ [**3-5**]. The weak reflection indicates the superstructure of α-phase of the parent compound $Bi_4V_2O_{11}$ [**1, 5**]. Except this weak super lattice reflection, all other reflections could be indexed with orthorhombic $Bi_4V_2O_{11}$ [**1**]. Moreover, the striking feature of the monoclinic pattern is the presence of a characteristic doublet at $2\theta \approx 45.5^o$ and 46.5^o which is a singlet in the orthorhombic pattern [**3, 6-8**]. As shown in **Fig. 5.1**, there is singlet at $2\theta \approx 45.5^o$ and 46.5^o which confirms that phase is orthorhombic. On the other hand, the

sample with composition x = 0.3, the splitting at $2\theta \approx 32°$ and 54° began to converge which indicates the partial suppression of α→β phase transition. Moreover, weak splitting of peak at ~ 32^o signifies small contribution of β-phase.

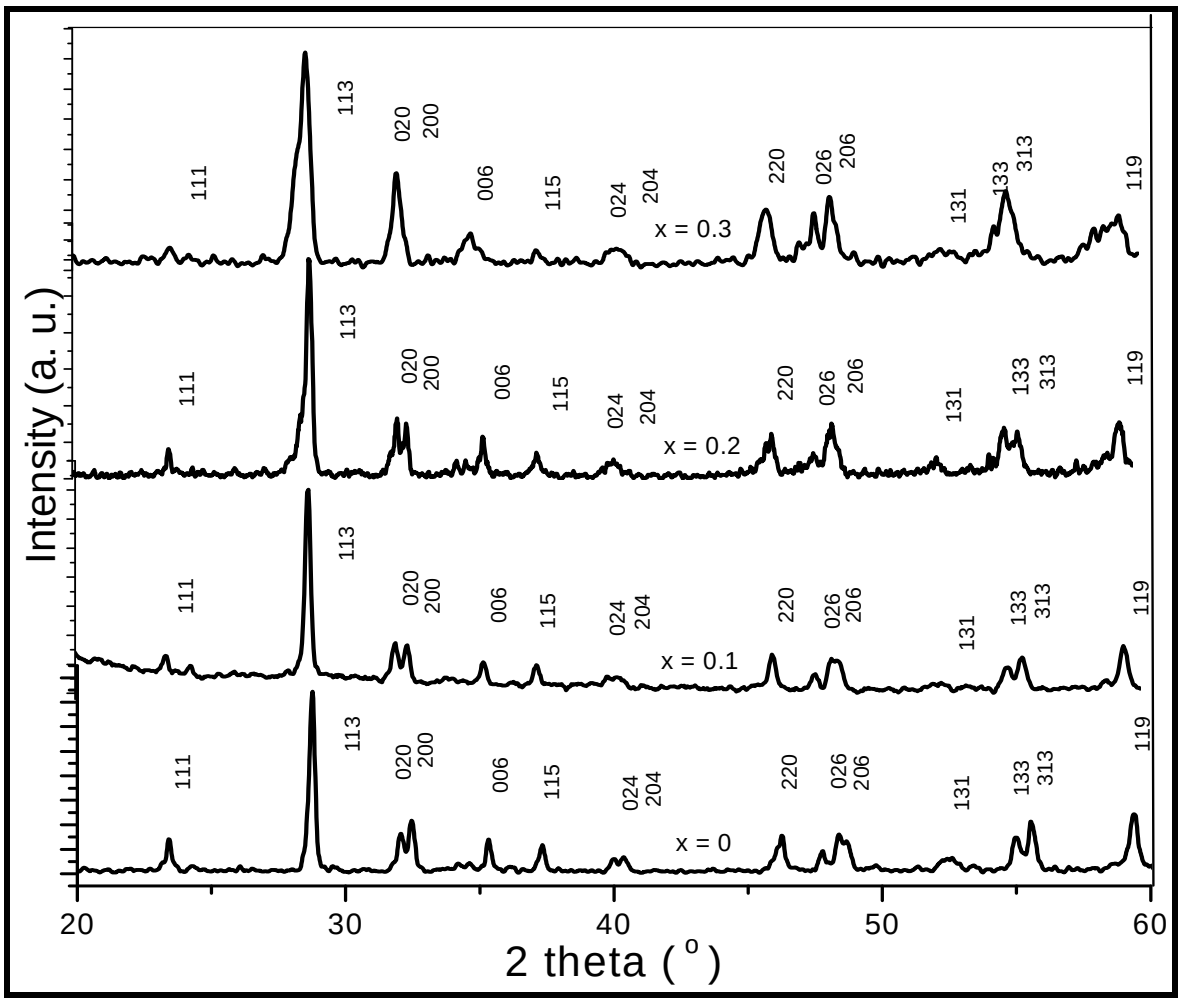

Fig.5.1: X-ray diffraction pattern of $Bi_{4-x}Ba_xV_2O_{11-\delta}$.

The composition dependence of unit cell parameter for the series compound has been shown in **Table 5.1**. The value of the unit cell parameter for the undoped compound as explain in the chapter III and IV agrees well with the values reported earlier by other researcher. It has been observed that, the value of the cell parameter *a* and *c* increases where as *b* decreases with the increase in dopant. This trend of change in the dimension of cell parameter is reported earlier as the sign of change from α to β polymorph [**9**]. The gradual increase of cell volume observed with increasing x is consistent with the substitution of smaller Bi^{3+} by the larger Ba^{2+} cations (1.03Å and 1.35Å respectively). On the other hand, it has been observed that Bi is more

electronegative (1.9) than both V (1.6) and Ba (0.9). Therefore, in respect of electronegativity it may be mentioned that there is possibility of Ba to substitute for V which will be further discussed in FTIR studies. The crystallite sizes of the compositions are found to be 47 nm, 23 nm, 25 nm and 26 nm respectively for the compositions x = 0, x = 0.1, x = 0.2 and x = 0.3 respectively

Table-5.1: Unit cell parameters of $Bi_{4-x}Ba_xV_2O_{11-\delta}$ series of compound.

composition	*a*(Å)	*b*(Å)	*c*(Å)	Volume(Å^3)
x = 0	5.521(20)	5.598(18)	15.243(22)	471.108
x = 0.1	5.543(18)	5.584(16)	15.246(14)	471.895
x = 0.2	5.564(15)	5.578(20)	15.252(13)	473.361
x = 0.3	5.575(17)	5.572(18)	15.258(16)	473.972

5.3.2. FTIR studies

The FTIR spectra of the pure (x =0) and doped compositions x = 0.1 and x = 0.4 are shown in **Fig.5.2**. Similar to the observed spectra for Li and Ca doped compounds (chapter II and IV), the position of the Bi-O bond for Ba doped compounds also remain same for all the compositions. This implies substitution of Ba for V rather than Bi and hence further supports the explanation concerning the electronegativity of the elements Bi, V, and Ba. On the other hand, the IR spectrum of the doped compound shows a decrease of fine structure in the vanadate anion regions. The Intensity of the IR peaks corresponding to the modes of vibration ν_{as} (V-O) in the region (~955 – 712 cm^{-1}) decreases with increase in Ba concentration. The fine structure corresponding to the asymmetric modes of vibration ν_{as} (O-V-O) in the regions (~670 – 500 cm^{-1}) decreases for x = 0.1 and finally almost disappears for x =0.4. Moreover, the IR spectrum of the doped compound shows a broadening of the sharp bands. The disappearance of fine structures and broadening of the sharp bands particularly in the vanadate anion region reveals crystallographic changes in local structures of the perovskite vanadate layer which give rise to the partial stabilization of β-polymorph.

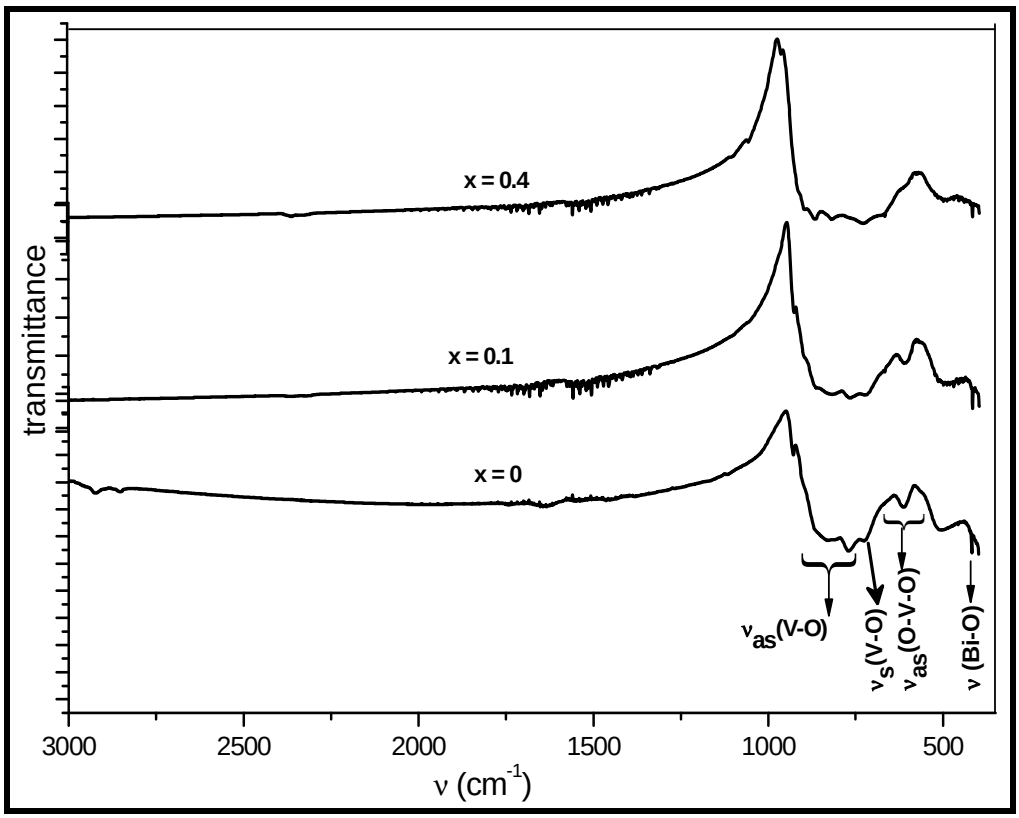

Fig.5.2: FT-IR patterns of $Bi_{4-x}Ba_xV_2O_{11-\delta}$ (x 0, 0.1, 0.4) series of compounds.

5.3.3. Microstructure analysis

The micro structural study on fractured surfaces of the samples was carried out under scanning electron microscopy (SEM) and the micrographs are shown in **Fig.5.3**. Samples with x = 0 exhibits fairly developed large grains with good grain to grain connectivity. However, some smaller grains are also found to be developed along with larger grains (~6 µm). SEM micrograph for x = 0.1 also shows larger grains in comparison to other doped specimens. For the specimens x = 0.3 and x = 0.4, small grain size were detected. Except the undoped sample, all the doped compositions exhibit the porosities which increase with the dopant concentration. The decrease in grain size and the existence porosities might be correlated with the lowering of sintering temperatures of the doped specimens with the substitution of barium. The

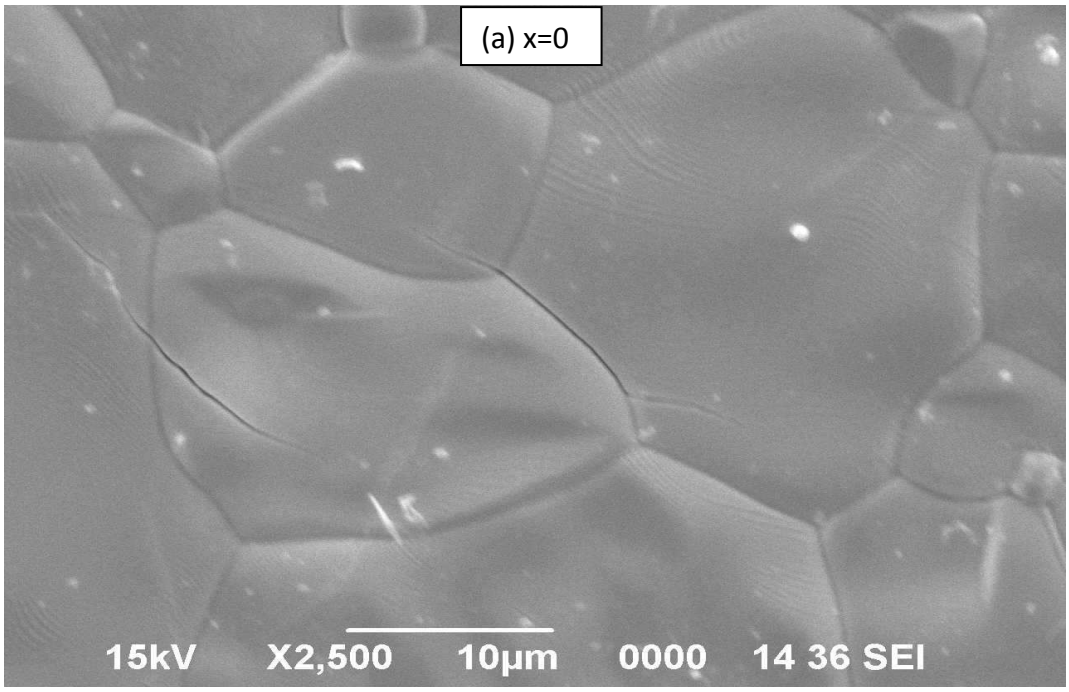

Fig. 5.3 (a): SEM micrograph of x= 0 composition of the series of compound $Bi_{4-x}Ba_xV_2O_{11-\delta}$.

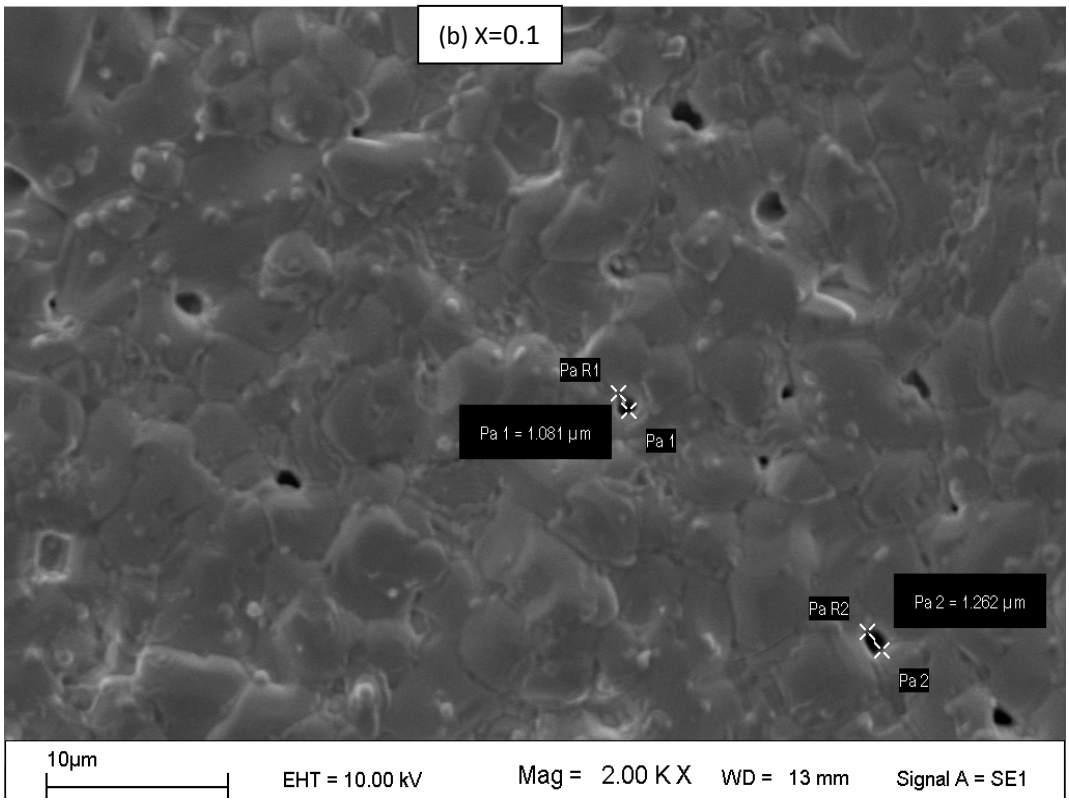

Fig. 5.3 (b): SEM micrograph of x = 0.1 composition of the series of compound $Bi_{4-x}Ba_xV_2O_{11-\delta}$.

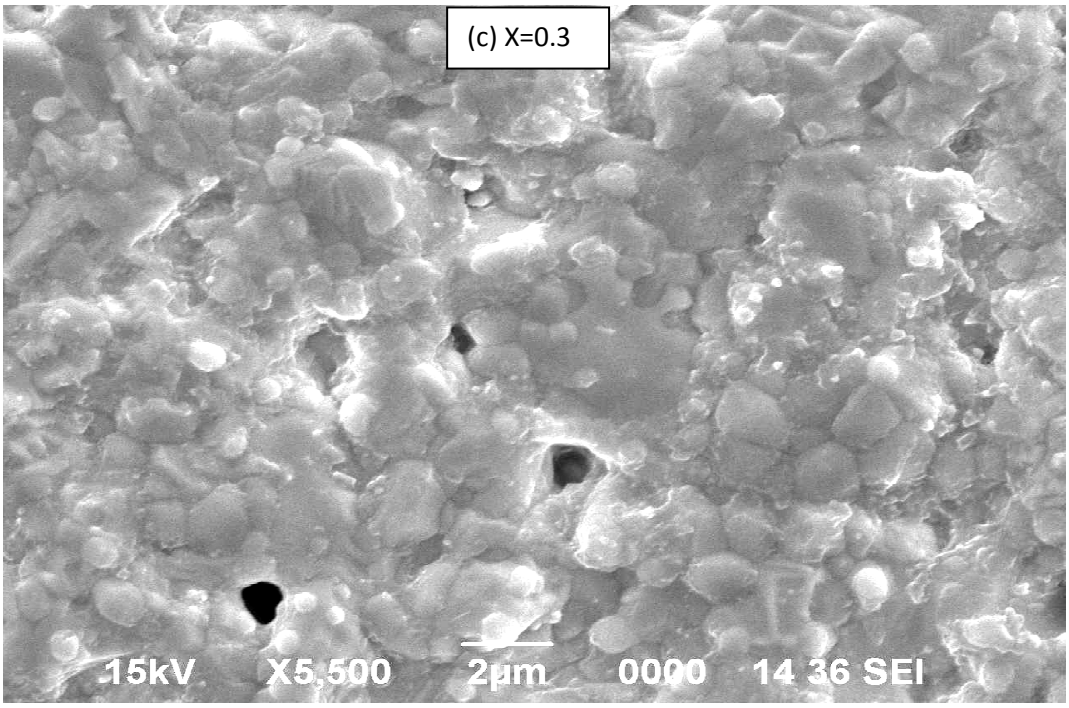

Fig. 5.3 (c): SEM micrograph of x = 0.3 composition of the series of compound $Bi_{4-x}Ba_xV_2O_{11-\delta}$.

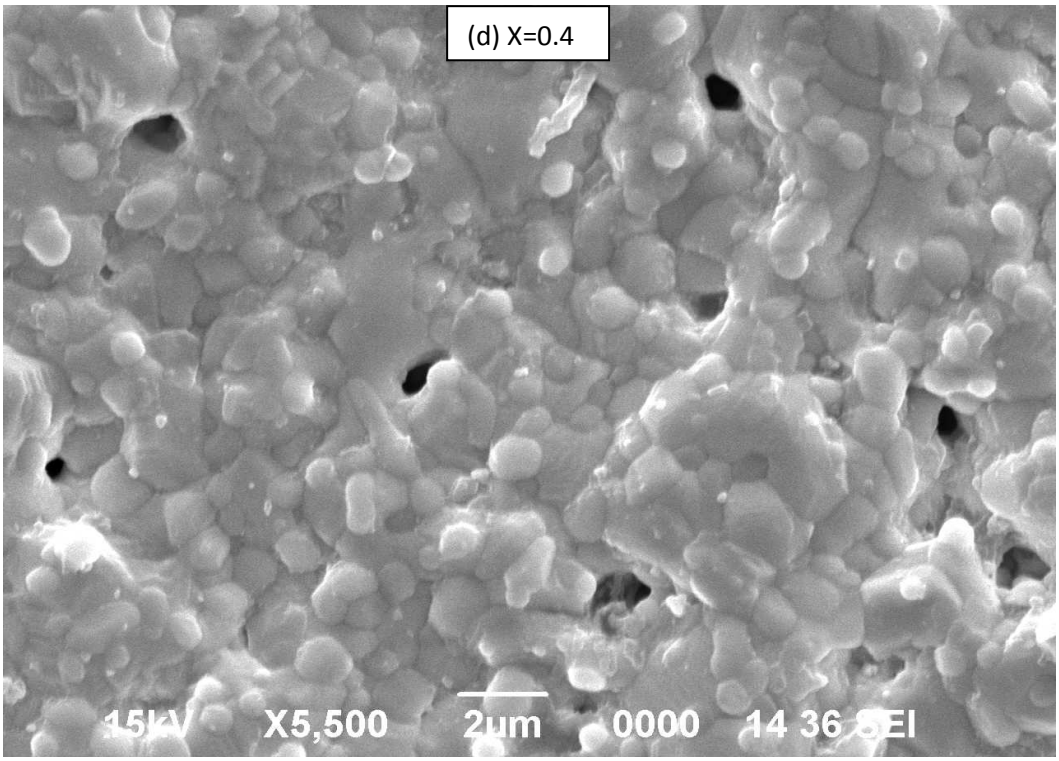

Fig. 5.3 (d): SEM micrograph of x = 0.4 composition of the series of compound $Bi_{4-x}Ba_xV_2O_{11-\delta}$.

variation in microstructural features for the specimens reflects the variation in conductivity between low and high conducting compositions. This may be attributed to clear grain formation of size (~5 μm) for high conducting composition x = 0.1 as compared to sample of low conducting samples (x = 0.3 and x = 0.4) with grain size of 2-3 μm. The grains of smaller size offer larger low conducting grain boundary area which is responsible for low conductivity.

5.3.4. Energy dispersive X-ray spectroscopy (EDS)

Energy-dispersive X-ray spectroscopy (EDS or EDX) technique is used to determine the elemental composition of the specimens. The EDS spectra of x-ray counts vs. energy (in keV) for the high and low conducting specimens x = 0.1, and x = 0.4 are shown in **Fig. 5.4**. To check the homogeneity of the sintered body, the pellets were broken into several pieces and EDS spectra were collected for each piece of the samples.

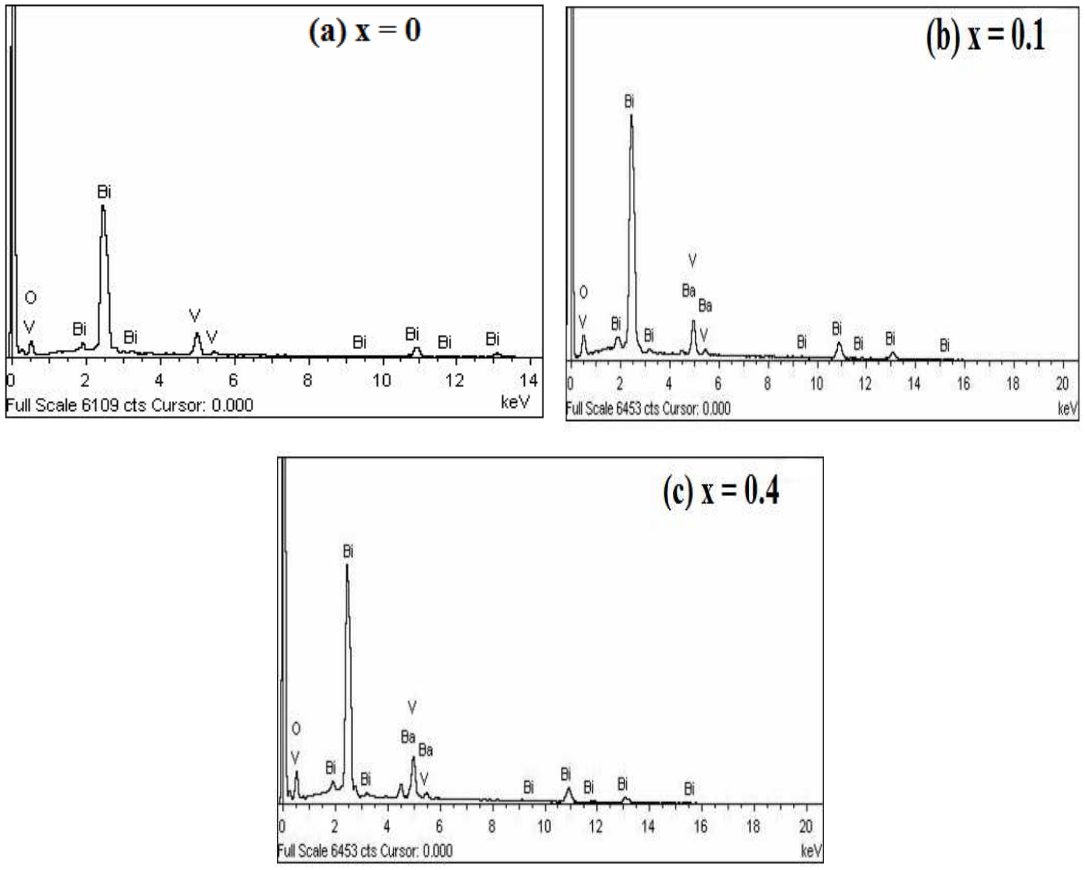

Fig. 5.4(a-c): EDS spectrum of (a) x = 0, (b) *x* = 0.1 and (c) x = 0.4 specimens of the series of compound $Bi_{4-x}Ba_xV_2O_{11-\delta}$.

The elemental compositions were found to be same for each sample at different inspected fields. The values of different elements obtained from the EDS studies along with the theoretically calculated values are tabulated in **Table 5.2**.

Table 5.2(a-c): Elemental content of different compositions of the series of compound $Bi_{4-x}Ba_xV_2O_{11-\delta}$.

(a) Elemental Content of x = 0 composition.

Element	Weight% (experimental)	Weight % (theoretical)
O	15.96	15.84
V	8.98	9.17
Bi	75.06	74.98
Totals	100.00	

(b) Elemental Content of x = 0.1 composition.

Element	Weight % (experimental)	Weight % (Theoretical)
O	15.47	15.64
Ba	2.56	2.45
V	9.24	9.1
Bi	72.73	72.79
Totals	100.00	

(c) Elemental Content of x = 0.4 composition.

Element	Weight % (experimental)	Weight % (Theoretical)
O	15.55	15.97
Ba	5.16	5.07
V	9.64	9.42
Bi	69.65	69.54
Totals	100.00	

It has been observed that the experimental values of the elemental content (atomic weight percent) of different compositions are found to be almost same with the theoretical values of the respective compounds which suggest that proper stoichiometry is maintained in the compositions.

5.3.5 DSC studies

Thermal analysis of $Bi_{4-x}Ba_xV_2O_{11-\delta}$; $0 \leq x \leq 0.4$ solid solutions for both heating and cooling cycles were carried out by differential scanning calorimetry (DSC) and representative plots are shown in **Fig. 5.5 (a-e).**

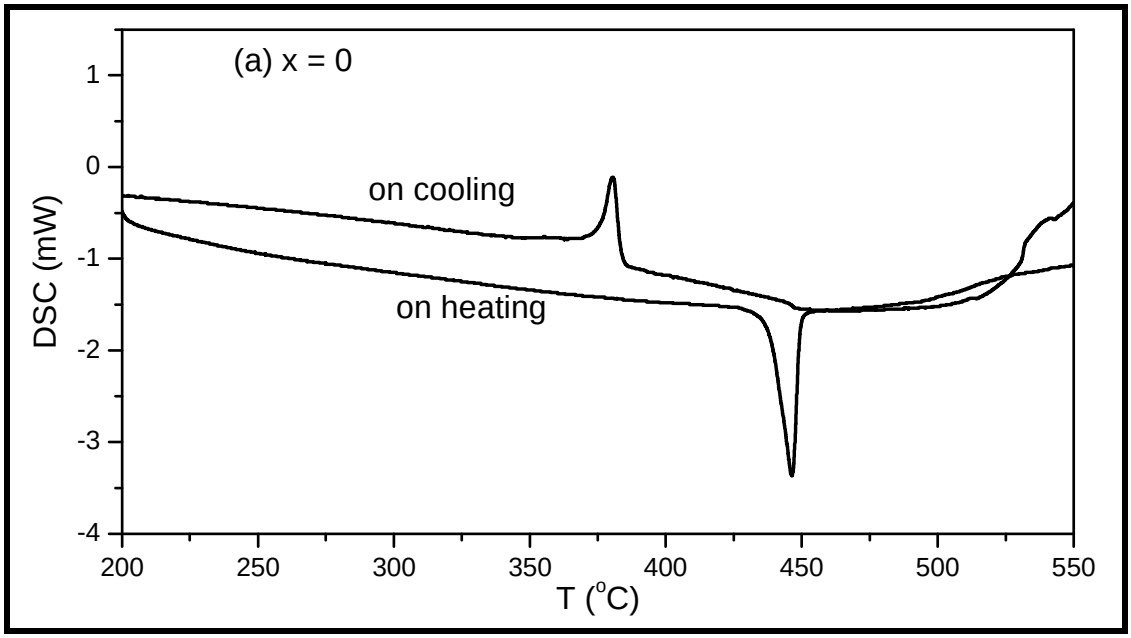

Fig. 5.5 (a): DSC plots for x = 0 composition of $Bi_{4-x}Ba_xV_2O_{11-\delta}$.

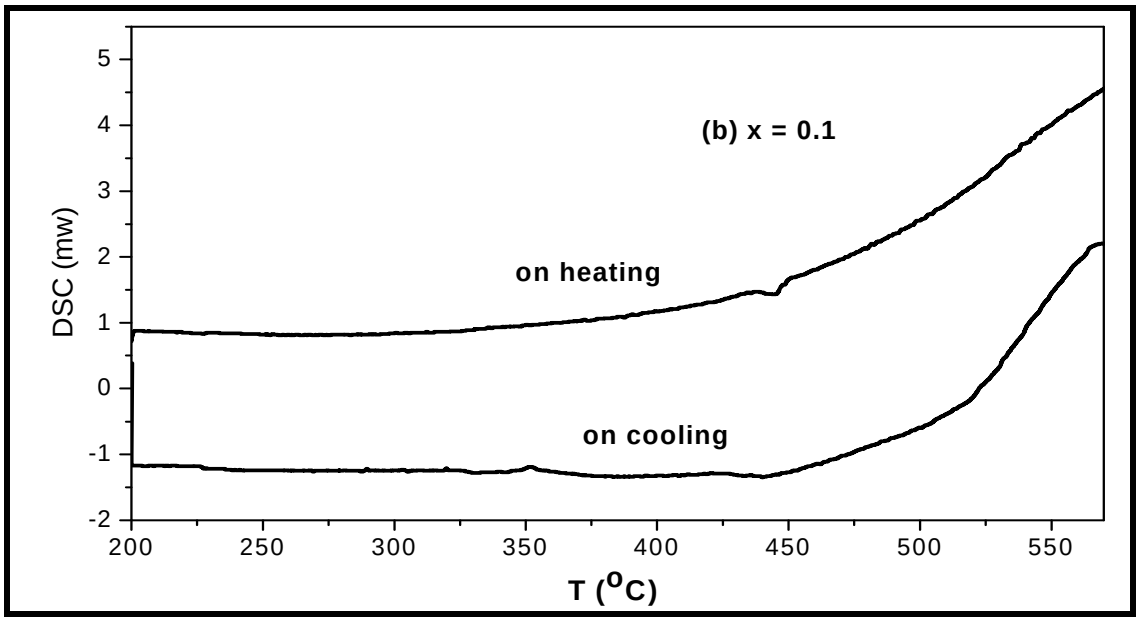

Fig. 5.5 (b): DSC plots for x = 0.1 composition of $Bi_{4-x}Ba_xV_2O_{11-\delta}$.

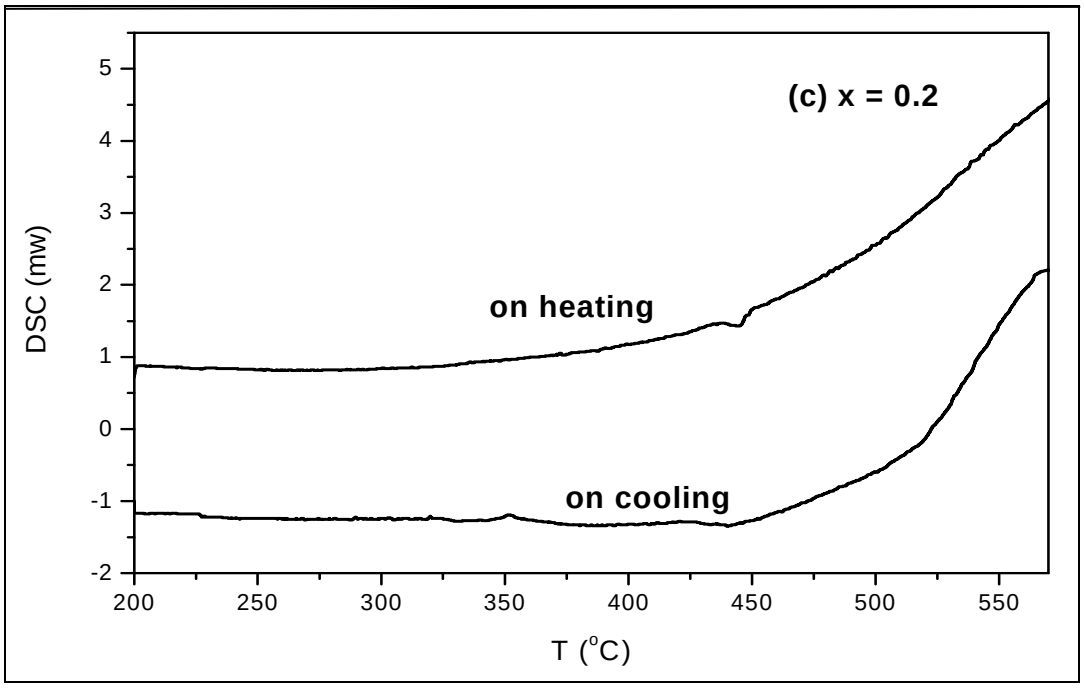

Fig. 5.5(c): DSC plots for x = 0.2 composition of $Bi_{4-x}Ba_xV_2O_{11-\delta}$.

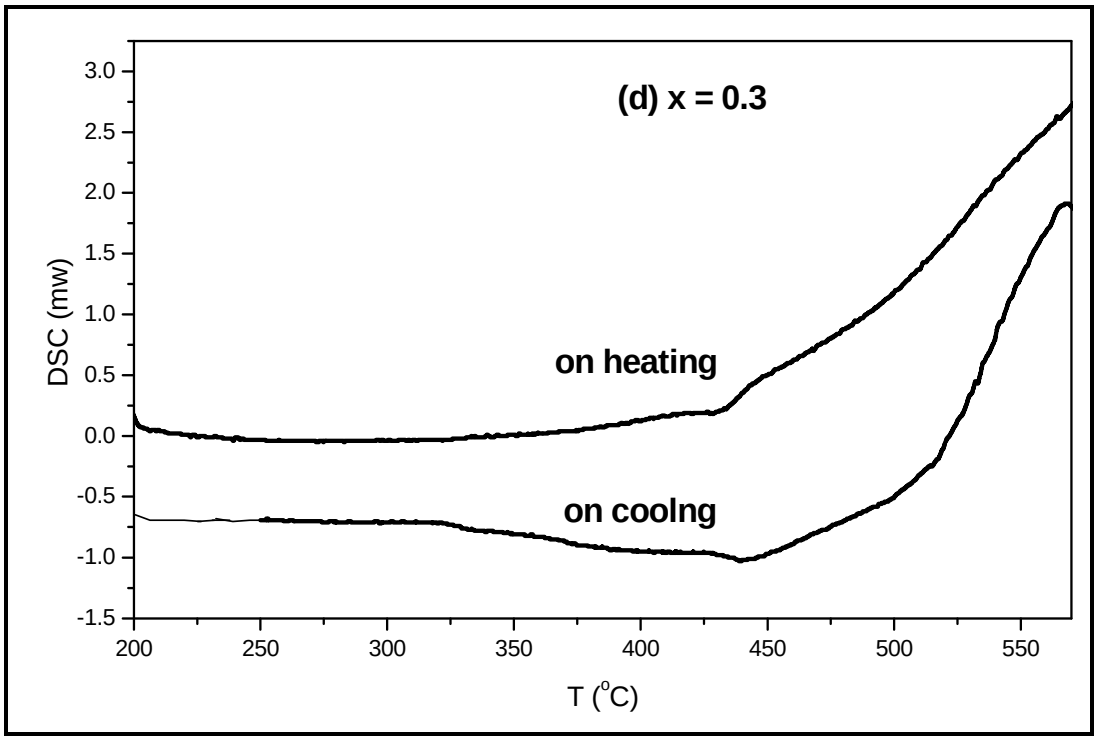

Fig. 5.5(d): DSC plots for x = 0.3 composition of $Bi_{4-x}Ba_xV_2O_{11-\delta}$.

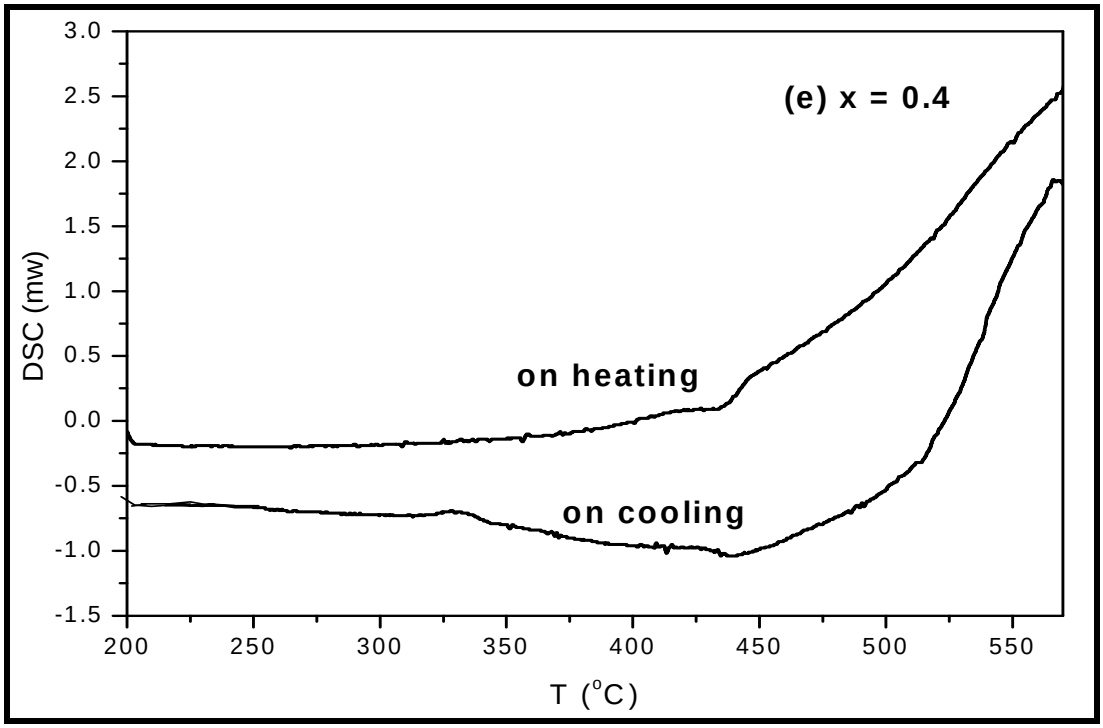

Fig. 5.5(e): DSC plots for x = 0.4 composition of $Bi_{4-x}Ba_xV_2O_{11-\delta}$.

Like other BIMEVOX compounds, both the doped and the undoped compounds show hysteresis behaviour [**10-12**]. The DSC plot representing the parent compound clearly indicates two endothermic peaks at 449 and 550 °C with. However, second peak is broader than first peak which means the second transition is sluggish with respect to the first transition. These transitions are due to α → β and β → γ phase change. Similar transitions were observed by other researcher also. On cooling the exothermic peak corresponding to α → β phase transition is observed at 368 °C.

It has been observed from **Fig. 5.5** that phase transition temperature goes on decreasing with the increase of dopant concentration. For the doped specimens the peaks representing α → β phase transitions are observed around 444, 440, 428 and 418 °C respectively for x = 0.1, 0.2, 0.3, and x = 0.4 compositions indicating partial suppression of $\alpha \rightarrow \beta$ phase transition. Upon cooling, the peaks representing $\alpha \rightarrow \beta$ phase transition shifted to 347 °C and 299 °C respectively for the specimens x = 0.1and x = 0.2. No exothermic peaks in the cooling cycle were observed for the compositions $x \geq 0.3$ indicating suppression of $\alpha \rightarrow \beta$ phase transitions for the compositions in cooling cycle. The values of the transition temperature, enthalpy and

transition width for different compositions of the compound $Bi_{4-x}Ba_xV_2O_{11-\delta}$ were calculated from the DSC analysis and are tabulated in **Table 5.3**.

Table 5.3: DSC peak analysis of $Bi_{4-x}Ba_xV_2O_{11-\delta}$ compound (Heating)

Composition (x)	T_r (^oC)	T (onset) (^oC)	T (offset) (^oC)	T_{off}-T_{on} (^oC)	enthalpy (J/gm)
0	446.36	439.91	449.04	9.13	8.35
0.1	444.09	459.38	449.54	9.84	6.98
0.2	440	428.88	444.14	15.26	3.51
0.3	428.98	428.27	443.91	15.64	1. 47
0.4	418	417.71	441.79	24.08	1.20

5.3.6 AC impedance analysis

Electrical conductivity was measured from the complex impedance spectra of the $Bi_{4-x}Ba_xV_2O_{11-\delta}$ (x = 0.1 to 0.4) samples. These impedance spectra were obtained by plotting imaginary part Z″ (ohm.cm) against the real part Z′ (ohm.cm) measured at different frequencies as shown by representative graphs in **Fig. 5.6 (a-d)** at 300 °C and 500 °C.

As depicted in **Fig. 5.6(a, c)**, the overall impedance spectra at low temperature (below ~ 450 °C) consist of two semicircular arcs along with an inclined spike. The high frequency arc of the semicircles attributed to the resistance within the grain of the materials and the semicircle in the low frequency side is due to the partial or complete blocking of charge carriers at the grain boundaries. At higher temperatures (above ~ 500 °C), the impedance spectra comprise of a single semicircular arc by which the contribution of bulk and grain boundary could not be differentiated. However, the low frequency spike becomes more prominent at high temperatures. The inclined spike at low frequency is associated with the electrode polarization and suggests that the compound is an ionic conductor [**3, 5-6, 10**]. From the figure, it is observed that the intersection of the semicircles with the real axis shifts towards the origin with the increase in temperature.

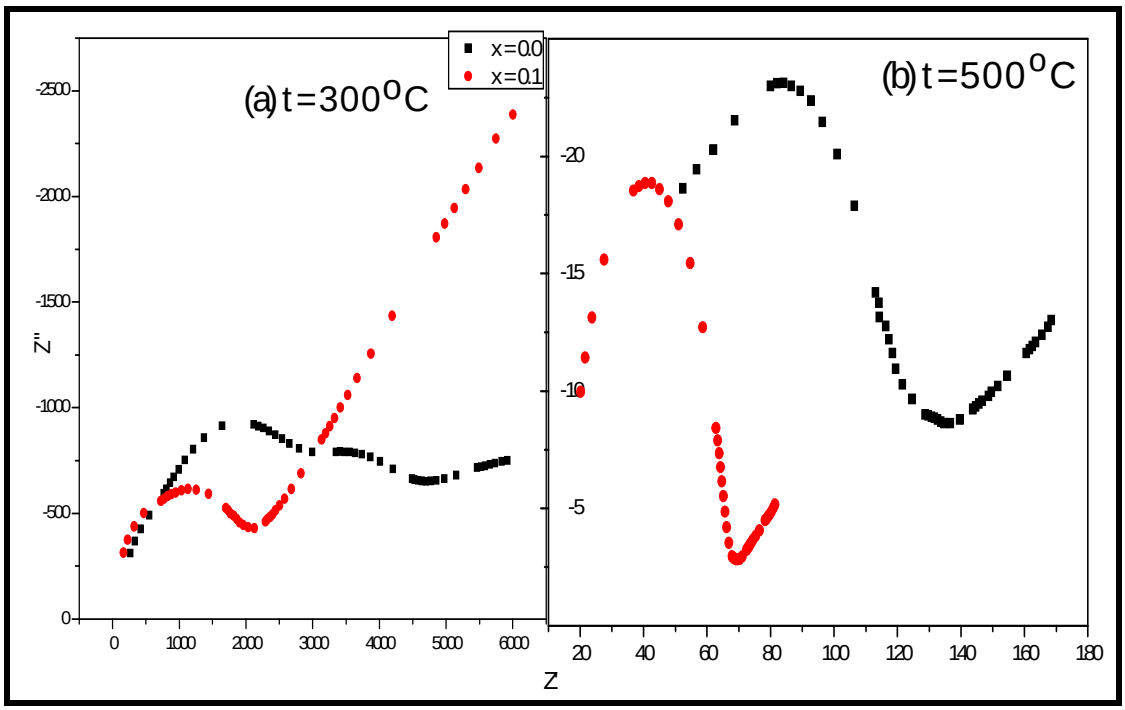

Fig.5.6 (a-b): Impedance spectra of $Bi_{4-x}Ba_xV_2O_{11-\delta}$ (x = 0 and 0.1) series of compound at temperatures 300 °C and 500 °C.

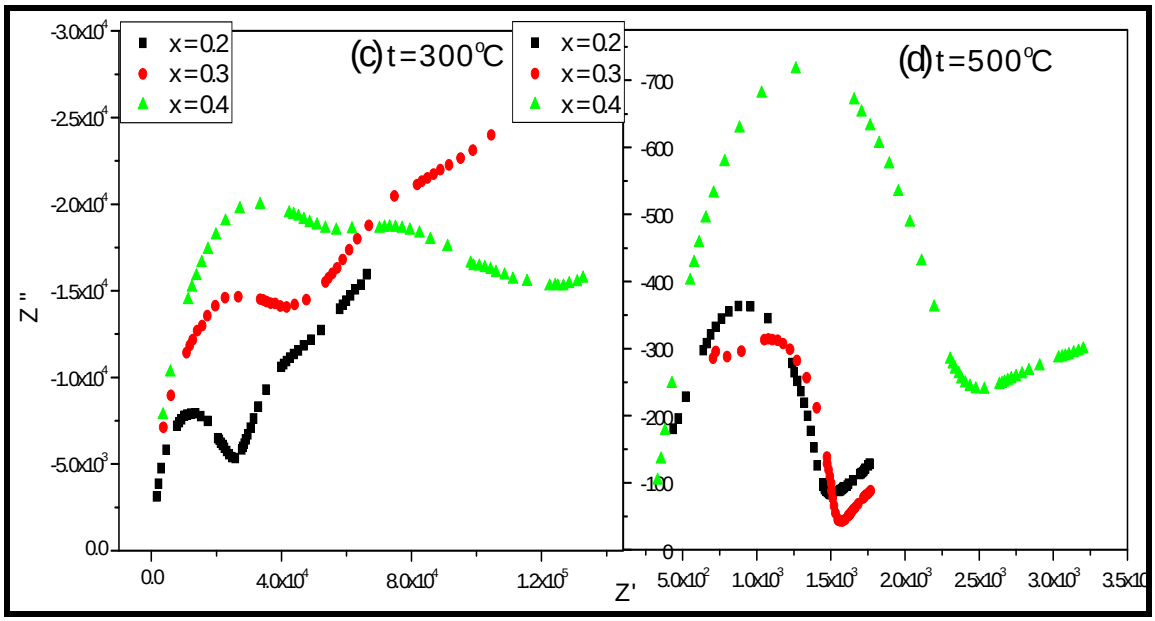

Fig.5.6 (c-d): Impedance spectra of $Bi_{4-x}Ba_xV_2O_{11-\delta}$ (x = 0.2, 0.3 and 0.4) series of compound at temperatures 300 °C and 500 °C.

5.3.7 Electrical conductivity analysis

The bulk conductivity of the pelletized samples is calculated with the help of the bulk resistance obtained from the analyzed impedance data at the various temperatures and pellet dimensions of the samples**. Fig.5.7** shows the log σ vs. 1000/T plots for all the dopant compositions ranging from x = 0 to x = 0.4. It has been observed that, the temperature dependence of conductivity obeyed the Arrhenius relation. The activation energy (Eg) is obtained from the slopes of the linear fit of the conductivity plot log σT vs. 1000/T.

The Arrhenius plot of conductivity for undoped $Bi_4V_2O_{11}$ and the doped compound with x = 0.1 composition (**Fig. 5.7**) shows three transition regions which can be correlated with the three principal polymorphs α, β and γ of $Bi_4V_2O_{11}$. Making a close similarity with the DSC results, the conductivity plots also reveals the suppression of phase transitions α → β corresponding to the compositions x = 0.1, 0.2, 0.3, and x = 0.4. The temperature dependent conductivity behaviour of the $Bi_{4-x}Ba_xV_2O_{11-\delta}$ series of compound ($0 \leq x \leq 0.4$) can usually divided into three regions - low temperature (below 440 °C), (2) intermediate temperature (440 – 520 °C) and high temperature region (above 520 °C). In the low temperature region the conductivity of x = 0.1 composition is significantly higher than the parent compound. The conductivity of the compounds with x > 0.1 gradually decreases with the increase of dopant concentration. In this temperature range, the conductivity of all the doped samples except for x = 0.4 is observed to be higher than the parent compound. In the intermediate range of temperature the conductivity of the composition x = 0.1 is still higher than the parent compound whereas the compounds with compositions x = 0.2, 0.3 and x = 0.4 exhibit lower conductivity than the undoped compound and gradually decreases with barium (Ba) concentration.

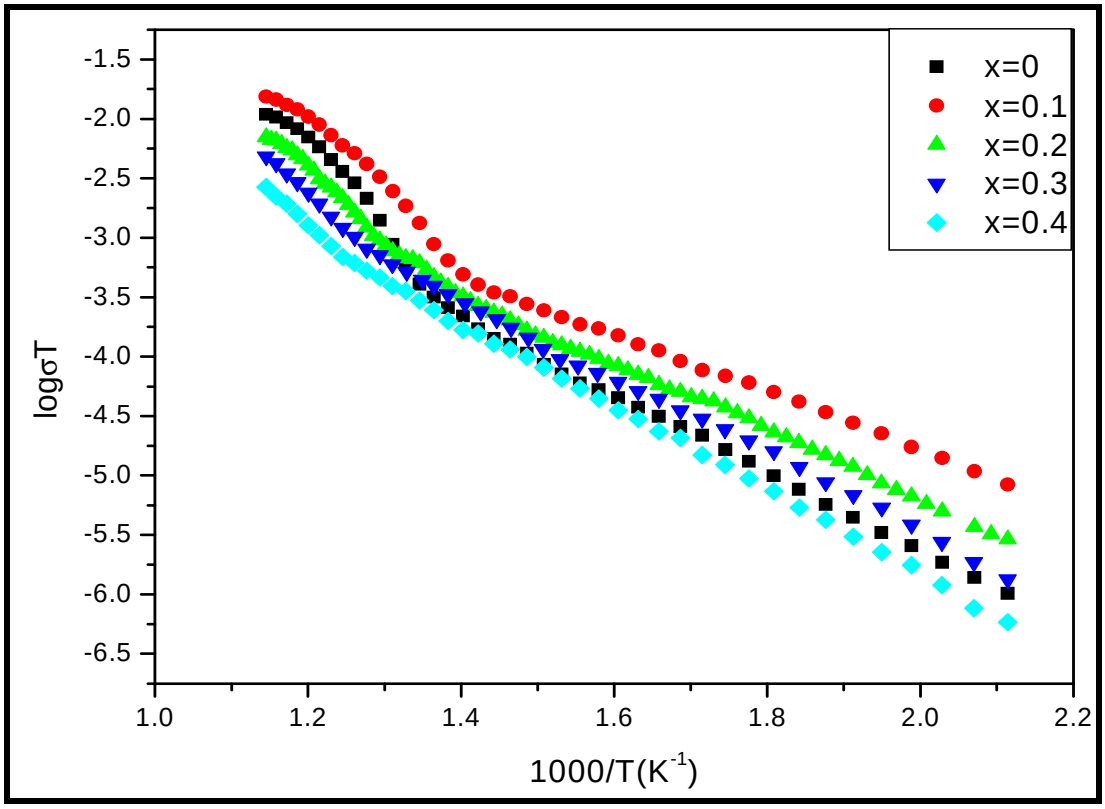

Fig.5.7: 1000/T vs. log (σ_{dc}) plot for Ba doped series of compound.

In the high temperature region, the conductivity of the doped specimens increases significantly with the increase of temperature. However, in this temperature range the conductivity of the specimens except x = 0.1 is observed to be lower than the parent compound. The highest ionic conductivity ($1.37x10^{-3}$ S/cm^{-1}) which is more than four times higher than the undoped compound is observed for x = 0.1 composition in the intermediate temperature domain at 460 ^{0}C. Higher ionic conductivity obtained for the doped compositions ($0 \leq x \leq 0.3$) in the low as well as intermediate temperatures is attributed to the excess oxygen ion vacancies created by aliovalent substitution. The highest ionic conductivity accounted for x = 0.1 composition can be correlated with the optimization of oxygen vacancies and the pathways between them [**13**]. On the other hand, the decrease of ionic conductivity for $x \geq 0.2$ compositions could be explained as a result of defect pair formation [**14**].

For the linear region below 400 ^{o}C, and above 500 ^{o}C, the values of activation energies (Eg) calculated from the linear fit of log σT vs 1000/T plot along with ionic

conductivities obtained from the d.c. conductivity plot for doped and undoped samples are summarized in **Table 5.4**.

Table 5.4: Conductivity (σ_{dc}) and activation energy (E_g) for the $Bi_{4-x}Ba_xV_2O_{11-\delta}$ series of compound.

Compound $Bi_{4-x}Ba_xV_2O_{11-\delta}$	σ_{dc} (Scm^{-1})		E_g (eV)	
	400 °C	500 °C	> 400 °C	> 500 °C
x=0	1.06×10^{-4}	1.4×10^{-3}	0.63	1.09
x=0.1	2.76×10^{-4}	3.25×10^{-3}	0.50	0.85
x=0.2	1.65×10^{-4}	9.48×10^{-4}	0.59	1.15
x=0.3	1.44×10^{-4}	7.12×10^{-4}	0.67	1.18
x=0.4	1.22×10^{-5}	4.62×10^{-4}	0.75	1.22

A representative plot of log σT vs 1000/T for the compounds of the series $Bi_{4-x}Ba_xV_2O_{11-\delta}$ below 400 °C is shown in the **Fig. 5.8**.

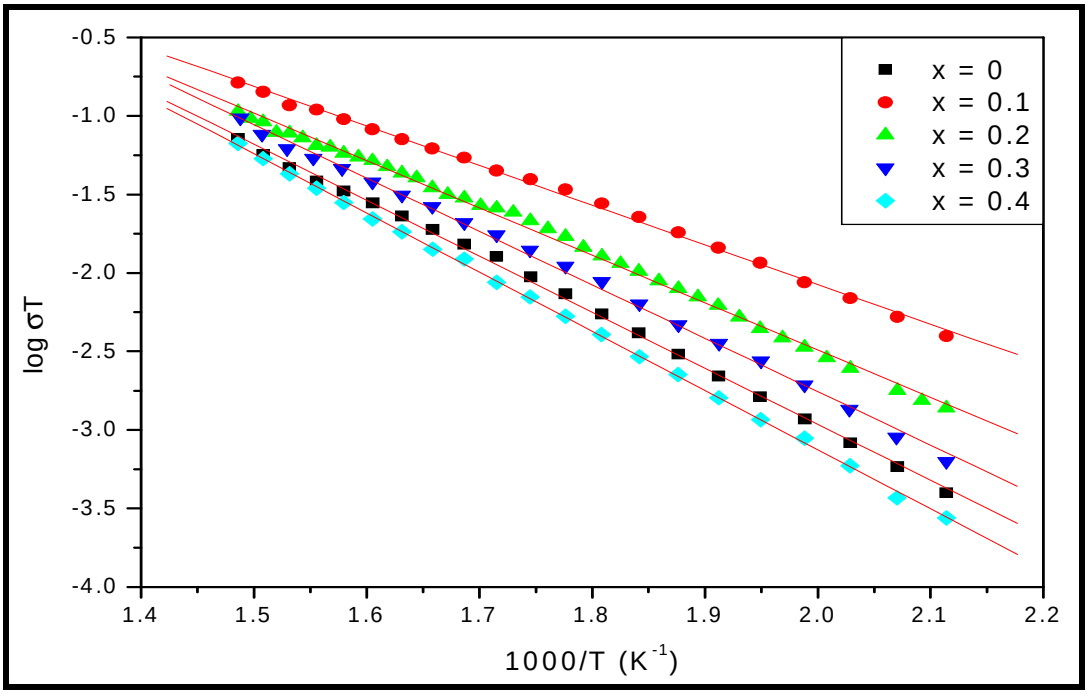

Fig. 5.8: 1000/T Vs log σT plots (below 400 °C) for $Bi_{4-x}Ba_xV_2O_{11-\delta}$ series of compound.

The variation of ionic conductivity is found to be in accordance with the activation energy calculated from the log σT vs 1000/T plots for all the compositions in the temperature range below 400 ^oC, and above 500 ^oC.

The substitution of Ba^{2+} on bismuth site may likely to compensate the charge in the Bi_2O_3 layers leading to additional oxide vacancies for $x \leq 0.1$. The lower conductivity values of the samples with compositions $x \geq 0.2$ may be correlated with the formation of defect pairs or $x \leq 0.1$ may be the true solid solution limit.

5.3.8. Dielectric permittivity studies:

5.3.8.1. Frequency dependence of the dielectric constants ε′and ε′′:

From the measured impedance data *Z′* and *Z″*, the real and imaginary part of the complex dielectric permittivity (ε′and ε′′) were calculated according to the equations 2.21 and 2.22 as explained in chapter **II**. **Fig. 5.9 (a-f)** shows the frequency dependence of the real and imaginary part of dielectric permittivity for the dopant compositions of x =0.0, x = 0.1 and x = 0.4 (parent, highest and lowest conducting samples). From the **Fig. 5.9,** it is observed that both ε′and ε′′show strong dispersion at low frequencies. With increase in frequency, both ε′and ε′′ decreases and attains a constant value at high frequencies. The strong dispersions at low frequencies exhibited by both the components of the complex dielectric constant, comes out to be

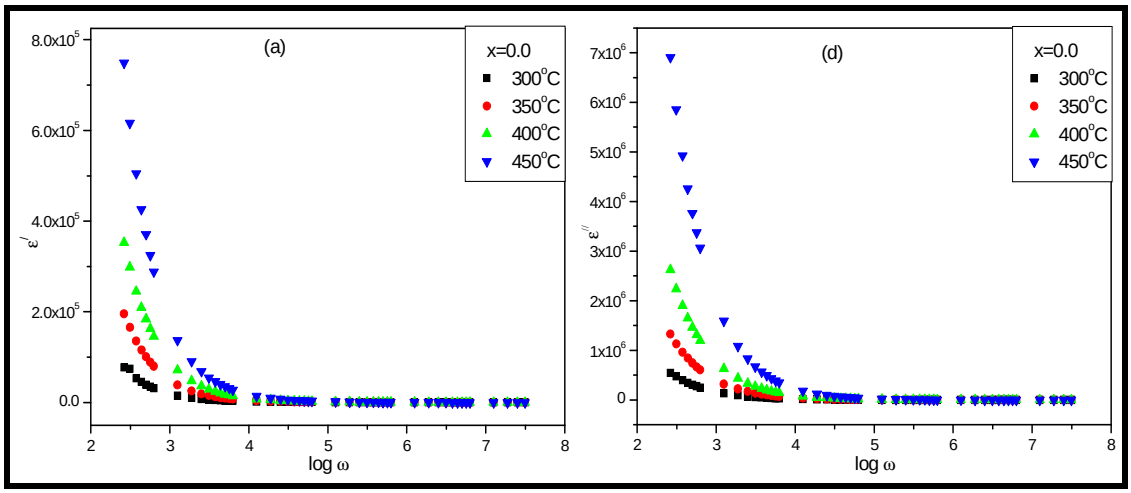

Fig. 5.9: The frequency dependence of ε′ (a) and ε″ (d) of $Bi_{4-x}Ba_xV_2O_{11-\delta}$ compounds for x = 0.0.

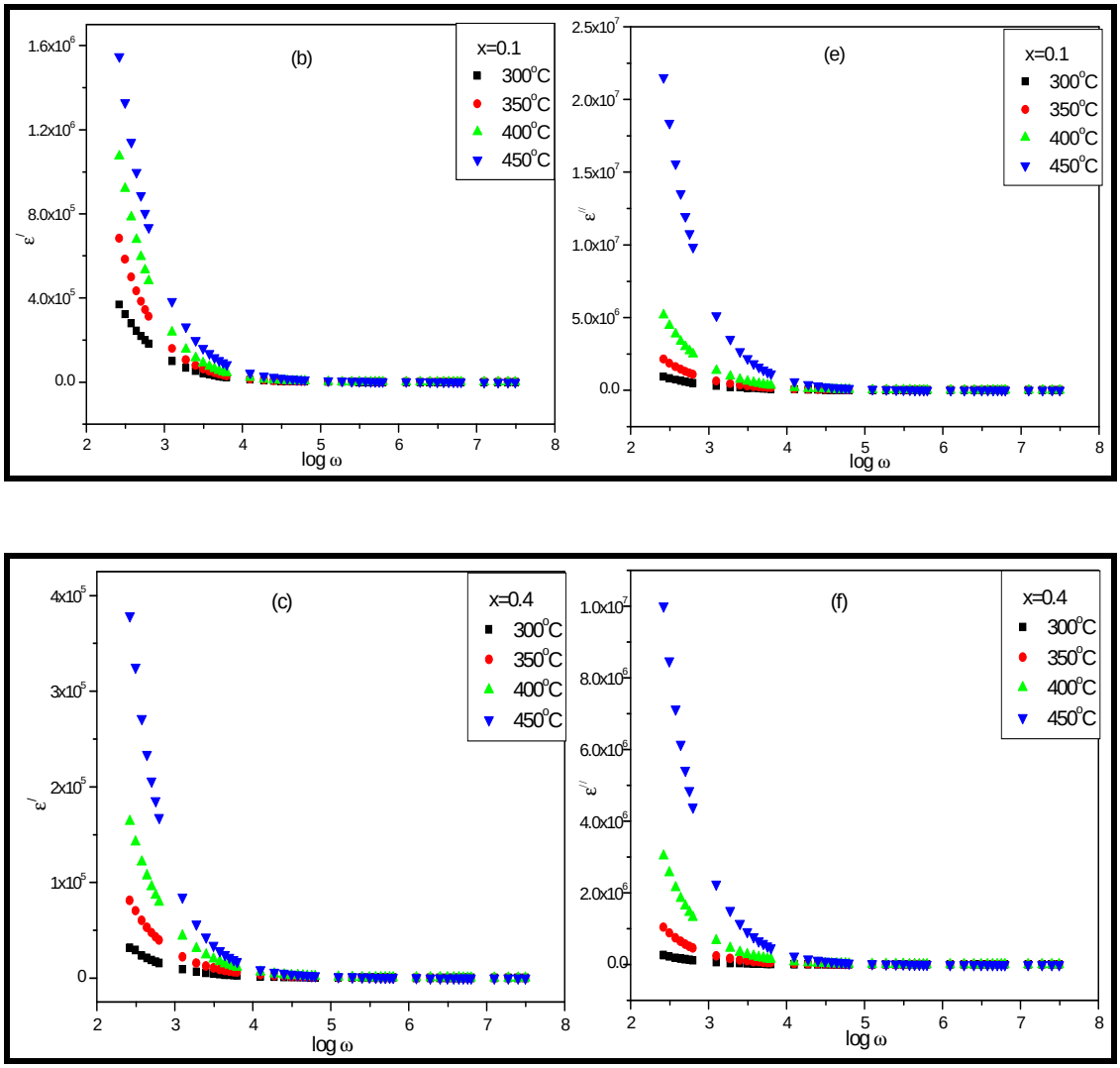

Fig. 5.9: The frequency dependence of ε′ (b, c) and ε″ (e, f) of $Bi_{4-x}Ba_xV_2O_{11-\delta}$ compounds for x = 0.1 and x = 0.4 compositions.

a common characteristic in ferroelectrics associated with good ionic conductivity which is referred to as low frequency dielectric dispersion (LFDD) [**6-8, 15**]. Due to the high periodic reversal of the a.c field at high frequencies, no charge have been accumulated at the interface and hence both ε′and ε″ remains constant, which can be explained in terms of the ion diffusion mechanism. On the other hand, at low frequencies, the charges get accumulated at the interfacial region that give rise to a net polarization of the ionic medium which result in the formation of space charge region at electrode-electrolyte interface and hence increases the dielectric constants[**16-17**]. It has been observed that the dispersion at low frequencies in the imaginary part of the

dielectric constant (ε′′) is stronger than that in the real part (ε′). This indicates the predominance of the dc conduction on ε′′in this frequency region **[15]**.

5.3.8.2. Temperature dependence of the dielectric constant:

The temperature dependence of dielectric permittivity of the system $Bi_{4-x}Ba_xV_2O_{11-\delta}$ for the compositions x = 0.0, 0.1, and x = 0.4 at different frequencies represented by the plots $\log\varepsilon_r$ vs. *T* is shown in **Fig. 5.10 (a-c)**. It has been observed that the dielectric

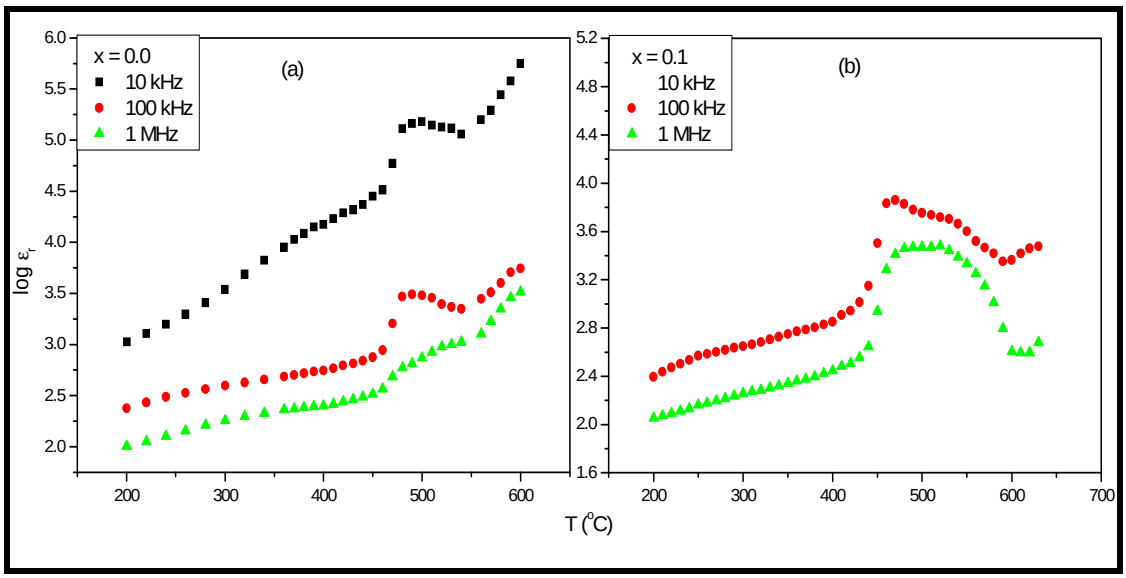

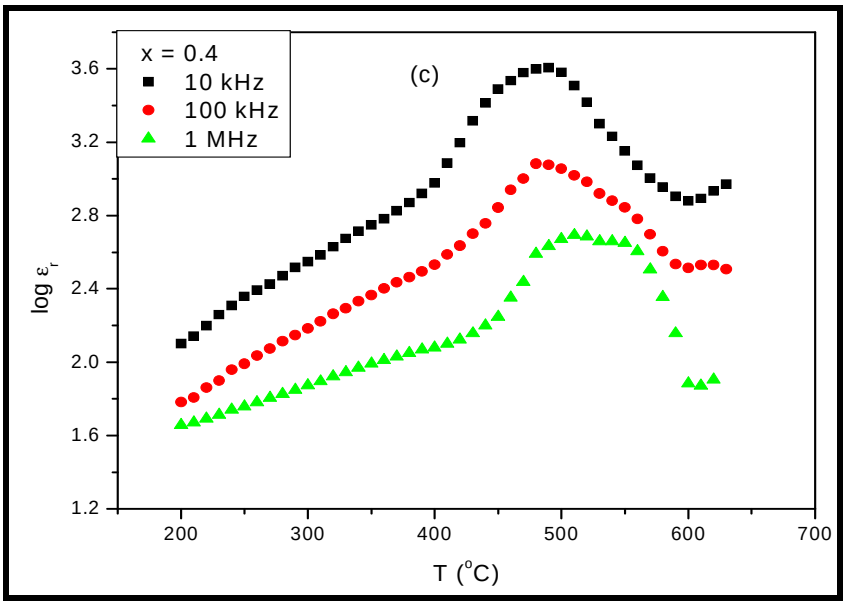

Fig. 5.10 (a-c): The temperature dependence of log ε_r of $Bi_{4-x}Ba_xV_2O_{11-\delta}$ compounds for x = 0.0, 0.1 and x = 0.4 compositions at different frequencies.

permittivity generally increases with increasing temperature, reaches a maximum corresponding to the phase change and then decreases. It is also found that the broadening of dielectric peaks for compositions with partially suppressed $\alpha \rightarrow \beta$ increases with increasing value of x. This is the characteristic of the increased diffusion of oxygen ion vacancies associated with an order disorder transition [**18-20**]. It has been observed that a strong dielectric dispersion begins from 200 °C and increases with increase in temperature. The dispersion is stronger near T_c (450 °C). The increase of ε_r above T_c at all frequencies under study, is as a consequence of another phase transition, which is reported to exist around 560 °C for some of the BIMEVOXes [**15,21-22**]. The appearance of anomaly near the transition temperature for all the samples under study reveals a coupling between space charge and ferroelectricity [**15**].

5.4 Conclusion:

1. The series of compounds $Bi_{4-x}Ba_xV_2O_{11-\delta}$ ($0 \leq x \leq 0.4$) have been synthesized by standard solid-state reaction technique.

2. Room temperature X-ray diffraction studies reveal partial suppression of phase transition for the doped sample.

3. SEM micrographs of the doped specimens exhibit porosities and small grain size which increases with the amount of Ba concentration. These facts might be correlated with the lowering of sintering temperatures of the doped specimens with the substitution of barium (Ba).

4. In good agreement with the XRD result, the DSC plots for the compounds exhibit partial suppression of $\alpha \rightarrow \beta$ phase transition.

5. The highest ionic conductivity (1.37×10^{-3} S/cm^{-1}) with respect to the parent compound is obtained for x = 0.1 composition in the intermediate temperature domain at 460 ^{0}C

6. The higher activation energy for the doped compositions with x > 0.1 makes oxygen ion migration more difficult and thereby decreasing the value of ionic conductivity.

7. The strong low frequency dispersion at low frequencies exhibited by the dielectric constants (both ε' and ε'') suggests ferroelectricity in the material.

8. The appearance of anomaly in the temperature (T) vs. Log ε_r plot near the transition temperature reveals a coupling between space charge and ferroelectricity.

References:

[1] S. Beg, N. A. S. Al-Areqi, S. Haneef, Solid state Ionics **179** (2008) 2260- 2264.

[2] M. Huve, R. N. Vannier, G. Nowogrocki, G. Mairesse and G. Van Tendeloo, J. Mater. Chem. **6** (1995) 1339.

[3] R. N. Vannier, G. Mairesse, F. Abraham, G. Nowogrocki, Solid State Ionics **80** (1995) 11-17.

[4] F. Krok, I. Abrahams, M. Malys, W. Bogusz, J. R. Dygas, J. A. G. Nelstrop, A. J. Bush, Solid State Ionics **136-137** (2000) 119-125.

[5] Yu. V. Emel'yanova, R. R. Shafigina, E. S. Buyanova, V. M. Zhukovskii, V. M. Zainullina, S. A. Petrova, Russian Journal of Physical Chemistry **80-11**(2006) 1725–1730.

[6] A. K. Jonscher, Phil. Mag. B **38** (1978) 587.

[7] A. K. Jonscher, D. C. Dube, Ferroelectrics **17** (1978) 533.

[8] Z. Lu, J. P Bonnet, J. Ravez, P. Hagenmuller, Solid State Ionics **57** (1992) 235.

[9] V. I. Voronkova, E. P. Kharitonova, O. G. Rudnitskaya, N. I. Sorokina, I. A. Verin, Crystallogr. Rep. **52** (2007) 316.

[10] B. A. Boukamp, Solid State Ionics **18-19** (1986) 136.

[11] J. Yam, M. Greenblatt, Solid State Ionics **81** (1995) 225-253.

[12] T. A. Nealon, Ferroelecttics **76** (1987) 377.

[13] R. Kant, K. Sing, O. P. Pandey, Ionic **16** (2010) 277-282.

[14] S. N. Achary, M. D. Mathews, S. J. Patwe, J. Tygi, J. Mater. Sci. Lett. **18** (1999) 355.

[15] K. Shantha, K. B. R. Varma, Solid State Ionics **99** (1997) 225-231.

[16] M. D.1ngram, Phys. Chern. Glasses **18** (1987] 215.

[17] D. L. Sidebottom, P. F.Green, R. K.Brow, J. Non-Cryst. Solids **183** (1995) 151.

[18] J. Yan and M. Greenblatt, Solid State Ionics **81** (1995) 225.

[19] Z. G. Yi, Q. F. Fang, X. P. Wang, G. G. Zhang, Solid State Ionics **160** (2003) 117.

[20] V. I. Voronkova, E. P. Kharitonova, O. G. Rudnitskaya, N. I. Sorokina, I. A. Verin, Crystallogr. Rep. **52** (2007) 316.

[21] K. B. R.Varma, G. N. Subbanna, T. N. Guru Row, C. N. R. Rao, J. Mater. Res. **5** (1990) 2718.

[22] F. Abraham, M. F. D. Gresse, G. Mairesse, G. Nowogrocki, Solid State Ionics, **28-30** (1988) 529.